Journal of Advanced Ceramics
2024, **13**(11): 1759–1770
https://doi.org/10.26599/JAC.2024.9220972

Research Article

$La_{0.5-x}Sc_xSr_{0.5}MnO_{3-\delta}$ cathodes for proton-conducting solid oxide fuel cells: Taking advantage of the secondary phase

Hailu Dai[1], Samir Boulfrad[2], Xinrui Chu[1], Yueyuan Gu[3], Lei Bi[3,✉], Qinfang Zhang[1,✉]

[1] *School of Materials Science and Engineering, Yancheng Institute of Technology, Yancheng 224051, China*
[2] *College of Science & Engineering, Hamad Bin Khalifa University, Doha 34110, Qatar*
[3] *School of Resource Environment and Safety Engineering, University of South China, Hengyang 421001, China*

Received: August 1, 2024; Revised: September 5, 2024; Accepted: September 15, 2024

Abstract: Designing high-performance cathodes is crucial for proton-conducting solid oxide fuel cells (H-SOFCs), as the cathode heavily influences cell performance. Although manganate cathodes exhibit superior stability and thermal compatibility, their poor cathode performance at intermediate temperatures renders them unsuitable for H-SOFC applications. To address this issue, Sc is utilized as a dopant to modify the traditional $La_{0.5}Sr_{0.5}MnO_3$ cathode at the La site. Although the solubility of Sc at the La site is restricted to 2.5%, this modest quantity of Sc doping can improve the material's oxygen and proton transport capabilities, hence improving cathode and fuel cell performance. Furthermore, when the doping concentration exceeds 2.5%, the secondary phase $ScMnO_3$ forms *in situ*, resulting in $La_{0.475}Sc_{0.025}Sr_{0.5}MnO_3$ (LScSM)+$ScMnO_3$ nanocomposites. Although the secondary phase is often considered undesirable, the high protonation capacity of $ScMnO_3$ can compensate for the low proton diffusion ability of LScSM. These two phases complement each other to provide high-performance cathodes. The nominal $La_{0.4}Sc_{0.1}Sr_{0.5}MnO_3$ is the optimal composition, which takes advantage of the excellent electronic conductivity and fast oxygen diffusion rates of LScSM, as well as the good proton diffusion capacity of $ScMnO_3$, to produce a high fuel cell output of 1529 $mW \cdot cm^{-2}$ at 700 °C. Furthermore, the fuel cell exhibited good operational stability under working conditions, indicating that $La_{0.4}Sc_{0.1}Sr_{0.5}MnO_3$ is a viable cathode choice for H-SOFCs.

Keywords: $LaMnO_3$; $ScMnO_3$; cathode; proton conductor; solid oxide fuel cells (SOCFs)

1 Introduction

The development of sustainable technology is needed to address the current energy and environmental challenges worldwide [1–5]. Different technologies have been presented in recent years [6–10], and fuel cells have drawn great interest because they can efficiently transform chemical energy into electricity while generating few pollutants [11,12]. Throughout the history of fuel cell research, various fuel cell types have been proposed, with two kinds receiving the greatest attention. One type consists of proton exchange membrane fuel cells (PEMFCs) [13], whereas the other consists of solid oxide fuel cells (SOCFs) [14]. Compared with PEMFCs, which employ polymer electrolytes and noble metal electrodes, SOFCs use ceramic oxides as the primary components [15,16], avoiding the use of expensive electrodes and liquid leakage, which has received significant attention [17–19]. However, the working temperature of traditional SOFCs is high (over 800 °C), causing numerous issues [20]. As a result, one of the most important tasks in the SOFC community is to lower the working temperature [21,22].

To respond to this call, proton-conducting SOFCs (HSOFCs) have been proposed [23,24]. Unlike traditional SOFCs, which employ oxygen-ion conducting electrolytes, H-SOFCs use proton-conducting electrolytes [25,26]. Because proton conductors have a lower activation energy than do oxygen ion conductors [27,28], the use of proton-conducting electrolytes allows SOFCs to operate at lower temperatures. Indeed, some oxygen-ion conducting SOFCs (O-SOFCs) still perform better than H-SOFCs do. However, the low activation energy of proton-conducting electrolytes makes the operation of H-SOFCs at low temperatures favorable. The performance of a fuel cell is influenced not only by its electrolyte but also by its electrodes. Compared with O-SOFCs, which have a long history, the development of H-SOFCs has flourished only recently. The search for and design of compatible materials are still ongoing, and some excellent cathodes have been proposed [29,30], greatly increasing the performance of H-SOFCs, which makes them sufficiently competent compared with O-SOFCs. Currently, research on H-SOFCs has become a hot topic in the field [31,32]. However, a lower working temperature results in sluggish cathode kinetics, resulting in high polarization resistance and affecting fuel cell performance [33,34]. As a result, the H-SOFC community has prioritized the development of appropriate cathode materials [35,36].

Various materials have been proposed over the last few decades, and some deliver excellent performance [37,38]. The protonation ability, which can increase the cathode reaction area and thus improve the cathode performance, is highly desirable for H-SOFC cathodes [39]. Because of the peculiar cathode reaction mechanism of H-SOFCs, the cathodes should be explicitly designed for this application. The development of new cathode

✉ Corresponding authors.
E-mail: L. Bi, lei.bi@usc.edu.cn, bilei81@gmail.com;
Q. Zhang, qfangzhang@ycit.edu.cn

materials is prompted by the fact that existing cathodes typically lack protonation capability, rendering cathodes unsuitable for H-SOFC applications [40]. However, some classic materials, such as Sr-doped $LaMnO_3$, have shown promise in practical applications because of their high chemical stability, thermal compatibility, and long-term stability [41]. It is fair to expect that the performance of traditional cathodes for H-SOFCs can improve if protonation is incorporated. Wu *et al.* [42] employed Zn to dope a $La_{0.5}Sr_{0.5}MnO_3$ cathode, allowing for better protonation and increased cathode and fuel-cell efficiency. Dai *et al.* [43] employed Sc to partially substitute for Mn, which increased the catalytic activity of $La_{0.5}Sr_{0.5}MnO_3$. All of these studies demonstrate that the performance of standard $La_{0.5}Sr_{0.5}MnO_3$ cathodes can be improved to meet the needs of H-SOFCs if proper tactics are used.

Notably, earlier research has focused mostly on B-site doping of ABO_3 perovskite for the $La_{0.5}Sr_{0.5}MnO_3$ cathode, whereas the A-site doping has received less attention. Certain dopants, such as Sc, can be employed at both the A and B sites [44]. Therefore, investigating the effect of A-site doping on the performance of $La_{0.5}Sr_{0.5}MnO_3$ cathodes for H-SOFCs is interesting. In the present study, Sc was utilized as a dopant at the A site to partially replace La in $La_{0.5}Sr_{0.5}MnO_3$. The solubility of Sc in $La_{0.5}Sr_{0.5}MnO_3$, the formation of the secondary phase, and their impact on the cathode and fuel cell performance were investigated.

2 Materials and methods

$La_{0.5-x}Sc_xSr_{0.5}MnO_{3-\delta}$ (x = 0.025, 0.05, 0.1, and 0.2) was synthesized via a sol–gel technique, with preparation details available elsewhere [45]. Metal nitrates were used as the starting materials, and they were mixed via a stochiometric ratio in a water solution. Citric acid was used as the complexing agent, and the molar ratio of citric acid was 1.5 times greater that of the cations. Then, ammonium solution was used to adjust the pH value to approximately 8, followed by evaporation of the water under stirring. The solution became viscous and started to burn, leading to the formation of ashes. The precursors were heated at 1000 °C for 3 h to produce the target material. For comparison, conventional $La_{0.5}Sr_{0.5}MnO_3$ (LSM) without Sc doping was made via the same method. X-ray diffraction (XRD) was used to determine the phase composition of the produced materials. Transmission electron microscopy (TEM) was used to investigate the morphology and structure of the material. The elemental distribution of the material was determined via the TEM mapping method. ECR measurements were performed to investigate the oxygen and proton diffusion capacities of the materials. Dense bars were prepared for the measurements, and the conductivities of the materials were measured with a digital meter via the DC four-probe method. By altering the testing environment from air to 50% air, the conductivity of the material changed, and the relaxation time reflected the degree of oxygen diffusion and surface exchange rates. Similarly, changing the testing environment from dry to humified air allowed the relaxation time to reflect the rates of proton diffusion and surface exchange. To gain insight into the material properties, first-principles calculations using the DFT approach were performed [46]. The VASP program was utilized. The cutoff energy was set to 520 eV, with a 4 × 4 × 4 k-point mesh. The U_{eff} value of 3.9 eV was applied to Mn. Additional computation specifications can be found in previous studies [47].

Fuel cells with the $BaCe_{0.7}Zr_{0.1}Y_{0.2}O_{3-\delta}$ (BCZY) proton-conducting electrolyte were used to test the performance of the $La_{0.5-x}Sc_xSr_{0.5}MnO_{3-\delta}$ cathodes in H-SOFCs. The proton conductor BCZY was produced via the sol-gel process. The NiO+BCZY anode powder was prepared by mechanically mixing NiO and BCZY at a weight ratio of 3 : 2 in an ethanol solution. Then, the solution was dried in an oven to evaporate the ethanol, forming the anode powder. The anode powder was pressed to form an anode substrate. The BCZY electrolyte powder was then pressed onto the anode substrate, which was cosintered at 1350 °C for 6 h to fabricate the half-cell. The $La_{0.5-x}$ $Sc_xSr_{0.5}MnO_{3-\delta}$ cathode slurries, which were made of the cathode powder, ethyl cellulose, and terpineol at a weight ratio of 10 : 1 : 10, were painted on the electrolyte surface and co-fired at 900 °C for 10 min, resulting in full cells. Ag paste was employed as a current collector at the cathode side for all the cells. As the anode was a Ni-based cermet, which is quite conductive, no current collector was applied to the anode. Silver adhesive paste was used as the sealing material, which was dried at 150 °C for 2 h before fuel cell testing. The cells were tested with wet H_2 as the fuel. The I-V and power density curves were recorded via an electrochemical workstation. Electrochemical impedance spectroscopy (EIS) was used to study the cell resistances under open circuit voltage (OCV) conditions with a frequency range from 1 MHz to 0.1 Hz. The microstructures of the fuel cells were studied by scanning electron microscopy (SEM).

3 Results and discussion

Figure 1(a) displays the XRD patterns of $La_{0.5-x}Sc_xSr_{0.5}MnO_{3-\delta}$ (x = 0.025, 0.05, 0.1, and 0.2). $La_{0.5-x}Sc_xSr_{0.5}MnO_{3-\delta}$ with x = 0.025, 0.05, 0.1, and 0.2 are named LScSM, LSc5SM, LSc10SM, and LSc20SM, respectively. The Sc element can be doped at the La or Sr sites [44]. If Sc is doped at the Sr site, the oxygen vacancy in the material could be reduced, considering the higher valence of Sc^{3+} than of Sr^{2+}, which might not be good for the catalytic activity of the cathode. Therefore, Sc was selected to be doped at the La site for this study. With x = 0.025, a pure-phase LScSM material can be obtained. In contrast, samples with x = 0.05, 0.1, and 0.2 present an apparent secondary phase identified as $ScMnO_3$. Moreover, the diffraction peak positions of the samples with x = 0.05, 0.1, and 0.2 at approximately 32.8° do not shift relative to those of the pure-phase LScSM, implying that more Sc cations cannot be fully incorporated into the LSM lattice and that the Sc-doping concentration at the A site is restricted to 0.025. The amount of the $ScMnO_3$ phase increases as the Sc doping concentration increases. Figure 1(b) displays the elemental distribution of LSc10SM. Aside from a homogeneous distribution of La, Sc, Sr, and Mn in some particles, some particles exhibit obvious accumulations of Sc and Mn, implying the formation of LScSM and $ScMnO_3$ composites. The XRD results further prove that the secondary phase is $ScMnO_3$.

XRD Rietveld refinements were used to investigate the crystal structure of the samples. The refinement patterns shown in Fig. 2 reveal that the samples are well fitted with reliability index factors of χ^2 = 1.47, 1.21, 1.43, 1.15, 1.26, and 1.28 for LSM, $La_{0.5-x}Sc_xSr_{0.5}MnO_{3-\delta}$ (x = 0.025, 0.05, 0.1 and 0.2), and $ScMnO_3$, respectively. The crystal structure of LSM/LSScM is cubic in the *Pm*-3*m* space group, whereas $ScMnO_3$ has a hexagonal crystal structure in the *P*63*cm* space group. The lattice parameters for the LSM and LScSM are $a = b = c$ = 3.835 and 3.816 Å, respectively. Sc doping reduces the lattice parameters of the unit cell, which can be attributed to the smaller ionic radius of Sc than that of La. Moreover, the lattice parameters for LScSM acquired in LSc5SM, LSc10SM, and LSc20SM are similar to those of pure LScSM, as are

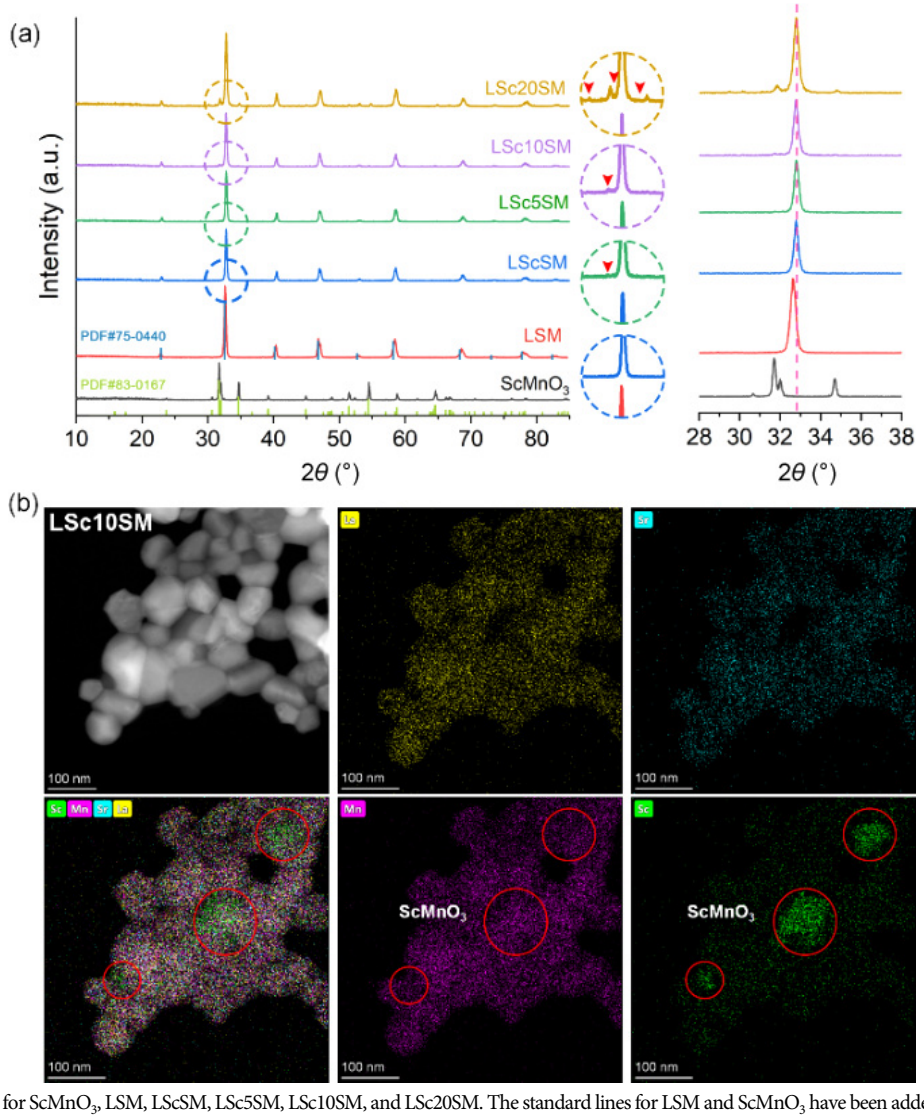

Fig. 1 (a) XRD patterns for $ScMnO_3$, LSM, LScSM, LSc5SM, LSc10SM, and LSc20SM. The standard lines for LSM and $ScMnO_3$ have been added as references. (b) TEM elemental mapping of LSc10SM.

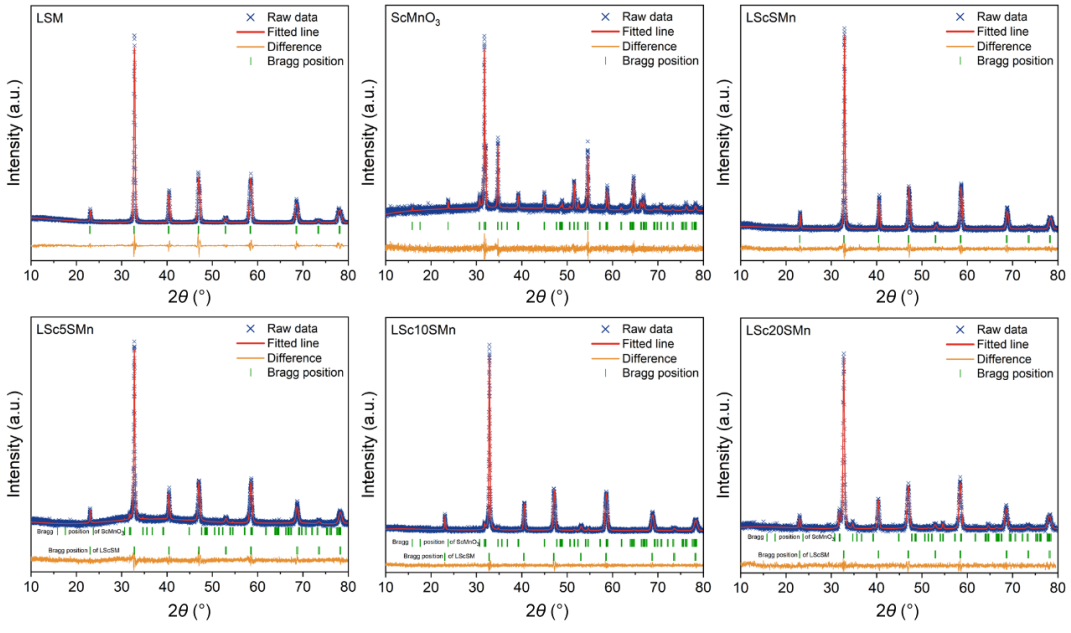

Fig. 2 XRD Rietveld refinements for LSM, $ScMnO_3$, LScSM, LSc5SM, LSc10SM, and LSc20SM.

清華大学出版社 Tsinghua University Press | SciOpen

the lattice parameters for $ScMnO_3$ produced in LSc5SM, LSc10SM, and LSc20SM. The weight ratios of LScSM and $ScMnO_3$ in LSc5SM, LSc10SM, and LSc20SM are 98.64% to 1.36%, 95.25% to 4.75%, and 86.35% to 13.65%, respectively, as indicated in Table 1. The weight concentration obtained from the refinement results is consistent with the ratio of LScSM and $ScMnO_3$ calculated according to the stoichiometric ratio. This result implies that with increasing concentrations of Sc in the $La_{0.5-x}Sc_xSr_{0.5}MnO_{3-\delta}$ system (x = 0.05, 0.1, and 0.2), the phase structure maintained LScSM and $ScMnO_3$, with no further incorporation of Sc into LScSM.

The high-resolution TEM (HRTEM) images in Fig. 3 provide a further demonstration of the results of the aforementioned refinement. The cubic structure in LSM, LScSM, and LSc10SM shows the crystallographic planes of (110), $(\bar{1}0\bar{1})$, and $(01\bar{1})$ with spacings of 2.715, 2.696, and 2.694 Å, respectively, and the calculated lattice parameters are 3.840, 3.813, and 3.810 Å, respectively. Moreover, $ScMnO_3$ in LSc10SM has a hexagonal structure with crystallographic planes of $(10\bar{2})$, $(\bar{1}0\bar{2})$, and $(00\bar{4})$. The corresponding spacings are 3.748, 3.748, and 2.795 Å, and the calculated lattice parameters are $a = b = 5.832$ Å and $c = 11.178$ Å. The HRTEM crystal structure and lattice parameters agree with the XRD results.

Nonetheless, a modest concentration of Sc (x = 0.025) can be incorporated into the LSM lattice. Therefore, investigating how Sc in the lattice affects the performance of the LSM cathode would be interesting. Before analyzing the pure-phase LScSM cathode for H-SOFCs, DFT calculations were performed to evaluate the material's atomic characteristics. Figures 4(a) and 4(b) illustrate the computed structure of the pure-phase LScSM, as well as the structure of the conventional LSM. Because the oxygen vacancy (Vo) is critical for cathodes, the Vo formation energies (E_{v_o}) for LSM and LScSM are determined according to $E_{v_o} = E_{defect} + \frac{1}{2}E_{O_2} - E_{perfect}$ [48], in which E_{defect} is the total energy of the defective bulk, E_{O_2} is the energy of O_2, and $E_{perfect}$ is the total energy of the stoichiometric bulk. The calculated findings show that E_{v_o} for LSM is 2.14 eV, whereas it is decreased to 0.59 eV for LScSM. The lower E_{v_o} indicates a reduced energy barrier to overcome, implying that doping Sc into LSM can facilitate Vo production and potentially benefit the cathode reaction. X-ray photoelectron spectroscopy (XPS) confirmed that Sc doping improved Vo formation in LSM. Figures 4(c) and 4(d) depict the XPS O 1s curves of LSM and LScSM. The ratio of oxygen species associated with oxygen vacancies (O_2^{2-}/O^-) to lattice oxygen (O_{lat}) has been shown to represent the material surface (Vo) [49,50]. The ratios for LSM and LScSM are 0.55 and 0.65, respectively, demonstrating that LSM has a higher Vo with Sc doping, which is consistent with the DFT calculations.

Table 1 Lattice parameters and weight ratios between LSM/LScSM and $ScMnO_3$ in $ScMnO_3$, LSM, LScSM, LSc5SM, LSc10SM, and LSc20SM

	Lattice parameter (Å)			wt% of LSM/LScSM	wt% of $ScMnO_3$
	LSM/LScSM	$ScMnO_3$			
	$a = b = c$	$a = b$	c		
LSM	3.835	—	—	100%	—
$ScMnO_3$	—	5.831	11.178	—	100%
LScSM	3.816	—	—	100%	—
LSc5SM	3.814	5.833	11.181	98.64%	1.36%
LSc10SM	3.815	5.830	11.175	95.25%	4.75%
LSc20SM	3.815	5.828	11.177	86.35%	13.65%

The protonation ability is particularly desirable for the cathode of H-SOFCs. Hence, the protonation ability of LSM with and without Sc doping was studied. In the presence of H_2O, H_2O molecules can be incorporated into the lattice, producing proton defects according to $H_2O + V_o^{\cdot\cdot} + O_o^x \rightarrow 2OH^{\cdot}$. Therefore, the hydration ability is used to evaluate the protonation of the material. The hydration energy ($E_{hydration}$) can be calculated according to $E_{hydration} = E_{2OH} - E_{defect} - E_{H_2O}$ [51], in which E_{2OH} is the energy of the crystal with two additional protons, E_{defect} is the total energy of the defective bulk, and E_{H_2O} is the energy of an H_2O molecule. $E_{hydration}$ of LSM and LScSM are determined to be 0.19 and −0.02 eV, respectively. The inclusion of Sc in LSM considerably reduces its $E_{hydration}$, making the hydration process more favorable. Furthermore, research on the oxygen and proton diffusion properties suggests that Sc doping may be beneficial. Figure 5(a) depicts the ECR curves of LSM and LScSM in an environment that transitions from air to 50% oxygen. The material conductivity varies as the oxygen partial pressure changes but eventually achieves a new equilibrium. The shorter the relaxation time is, the greater the oxygen diffusion ability is [52]. The relaxation time for LScSM is shorter than that of LSM, indicating that LSM with Sc-doping has enhanced oxygen diffusion kinetics. Fitting the ECR curves yields the oxygen diffusion coefficient (D_o) and surface exchange coefficient (k_o) values, as shown in Fig. 5(b). Both k_o and D_o values of LScSM are greater than those of LSM, indicating that LScSM has higher oxygen diffusion and surface exchange rates than the Sc-free LSM does. Additionally, doping Sc into LSM improves the proton diffusion kinetics. Figures 5(c) and 5(d) depict the ECR curves of LSM and LScSM in a humidified atmosphere. When H_2O is added to the atmosphere, the conductivity changes due to the exchange of charge carriers, assuming that the material possesses protonation capacity [53]. No conductivity change is found for LSM under such conditions, implying that no protonation occurs for LSM, which is consistent with Ref. [54]. In contrast, LScSM exhibits a change in conductivity, showing that protonation occurs there. This result is consistent with the low $E_{hydration}$ value of LScSM. However, the relaxation period of approximately 4000 s suggests that the proton diffusion rates are low. The proton

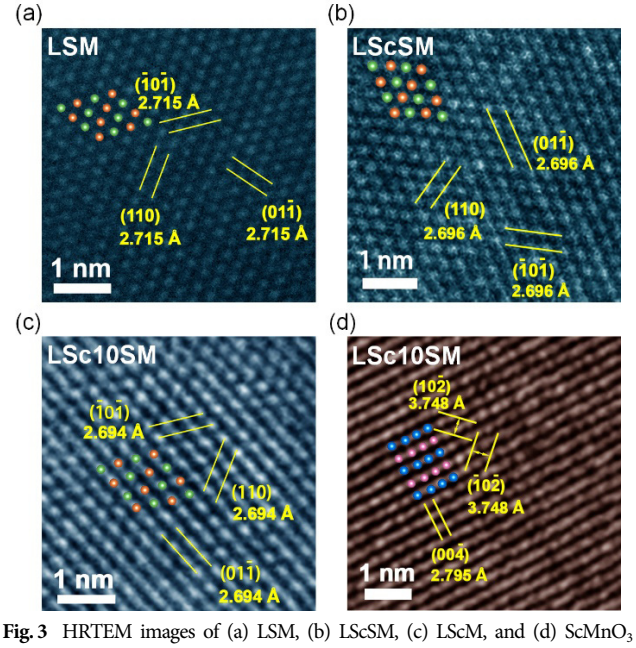

Fig. 3 HRTEM images of (a) LSM, (b) LScSM, (c) LScM, and (d) $ScMnO_3$ phases in LSc10SM.

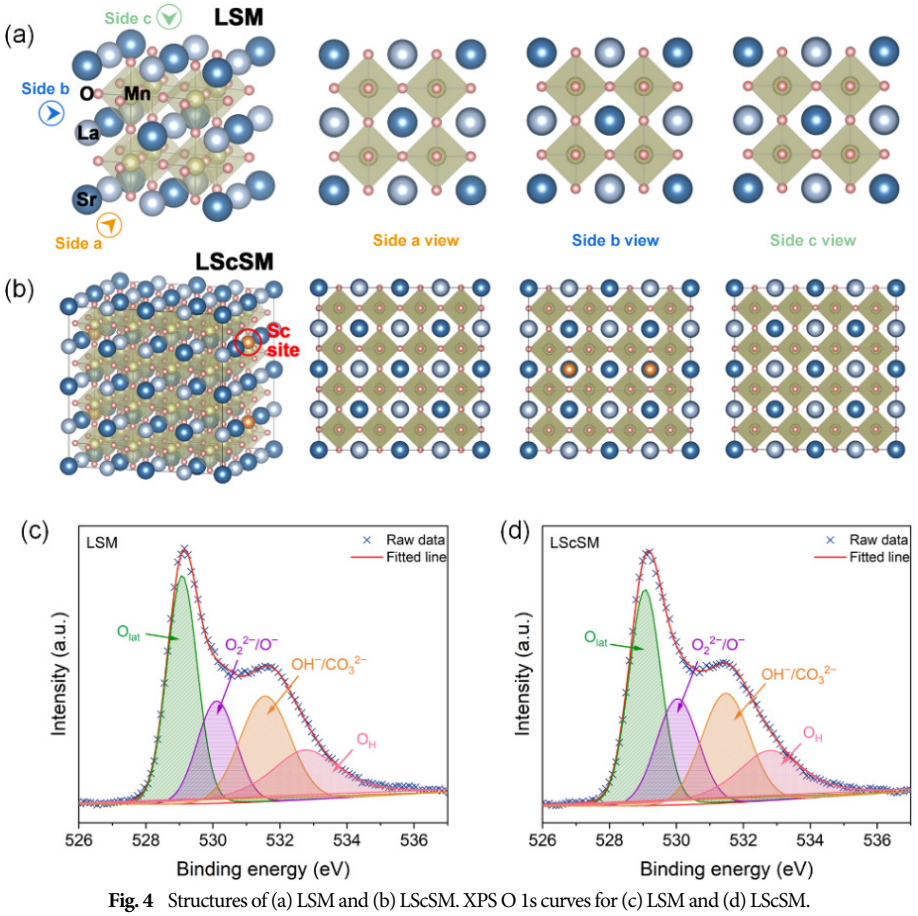

Fig. 4 Structures of (a) LSM and (b) LScSM. XPS O 1s curves for (c) LSM and (d) LScSM.

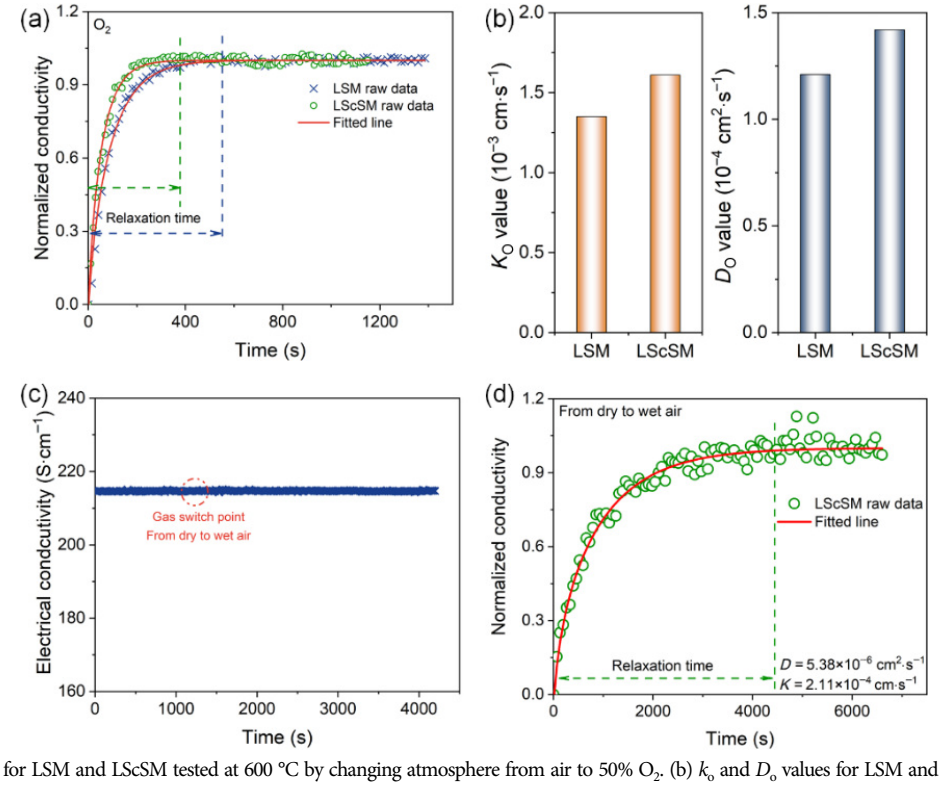

Fig. 5 (a) ECR curves for LSM and LScSM tested at 600 °C by changing atmosphere from air to 50% O_2. (b) k_o and D_o values for LSM and LScSM. ECR curves for (c) LSM and (d) LScSM tested at 600 °C by chaning atmosphere from dry to wet air. Humidity of wet air is approximately 3%.

diffusion coefficient (D_H) and surface exchange coefficient (k_H) of LScSM are 5.38×10^{-6} and 2.11×10^{-4} cm·S^{-1}, respectively. Although LScSM has a low proton diffusion rate, it is significantly better than standard LSM, which has no proton diffusion.

It is reasonable to expect LScSM to outperform the standard LSM for H-SOFCs because of its superior Vo, increased hydration potential, and faster oxygen and proton diffusion rates. Figures 6(a) and 6(b) illustrate the fuel cell performance of H-SOFCs with pure-phase LSM and LScSM cathodes. The peak power density (PPD) of the LSM cell is 303, 488, and 693 mW·cm^{-2} at 600, 650, and 700 °C, respectively. The comparatively low performance of LSM cell demonstrates that using a conventional LSM is not an optimal strategy for H-SOFCs. In contrast, using the LScSM cathode improved the fuel cell performance to 511, 708, and 930 mW·cm^{-2} at 600, 650, and 700 °C, respectively, for the same cell, indicating that the LScSM cathode may alleviate the low performance of LSM. The EIS measurements show the resistances of both cells, as illustrated in Figs. 6(c) and 6(d). The ohmic resistances (R_o) of LSM and LScSM cells are similar, measuring 0.129 and 0.127 Ω·cm^2, respectively. The very close R_o is expected because both cells employ the same half-cells with the same electrolyte thickness and have similar structures, as illustrated in Figs. 6(e) and 6(f). Some pores can be observed at the electrolytes, but these pores are close pores that are not connected, which cannot provide channels for gas diffusion and, therefore, cannot lead to gas leakage. OCVs for the LSM cell are 1.03, 1.01, and 1 V at 600, 650, and 700 °C, respectively, whereas OCVs for the LScSM cell are 1.04, 1.01, and 1 V at 600, 650, and 700 °C, respectively. These values are similar to the OCV values reported for H-SOFCs [17,39,40], suggesting that the close pores do not significantly decrease OCV. In contrast, the polarization resistance (R_p), which reveals electrode responses, varies between these two cells. The LSM and LScSM cells have R_p values of 0.12 and 0.084 Ω·cm^2, respectively. As both cells have the same Ni+BCZY anode, the difference in R_p is primarily due to the cathode. As a result, the increased cell performance is mostly due to the superior performance of the LScSM cathode compared with that of the conventional LSM cathode. However, it should be emphasized that while the pure-phase LScSM cathode can increase performance, the fuel cell performance remains lower than that of many reported cathodes [55,56], suggesting the need for further modification.

Considering the $La_{0.5-x}Sc_xSr_{0.5}MnO_{3-\delta}$ (x = 0.025, 0.05, 0.1, and 0.2) material system, the aforementioned phase study reveals that the secondary phase $ScMnO_3$ emerges when $x > 0.025$, resulting in the $ScMnO_3$+LScSM composite. Although attaining a pure phase material is normally the goal, several recent studies have shown that the formation of a second phase due to a solubility limit is not necessarily detrimental to cathode performance [57]. The new phase generated *in situ* can aid in the cathode reaction if it has adequate catalytic activity [58,59]. As a result, it would be very interesting to evaluate whether the secondary phase $ScMnO_3$ exhibited sufficient cathode catalytic activity in this study. DFT calculations were utilized to investigate E_{vo} and $E_{hydration}$ of $ScMnO_3$. The predicted E_{vo} and $E_{hydration}$ values are 3.04 and −0.17 eV, respectively. The relatively high E_{vo} value suggests that the Vo production is not viable in $ScMnO_3$. In contrast, $E_{hydration}$ is low, implying that $ScMnO_3$ has excellent hydration properties.

Experimental tests are conducted to demonstrate the prediction based on DFT calculations. Figure 7(a) shows the XPS O 1s curve for $ScMnO_3$. The proportion of oxygen species linked to oxygen vacancies and lattice oxygen is 0.47, which is lower than not only LScSM but also traditional LSM, implying that the Vo content in $ScMnO_3$ is lower than that in pure-phase LScSM and traditional LSM. Figures 7(b) and 7(c) present the results of the ECR measurements used to evaluate the diffusion of oxygen and protons. The relaxation time for $ScMnO_3$ in an environment changed from air to 50% O_2 is approximately 2000 s, which is much longer than the relaxation time for LSM and LScSM,

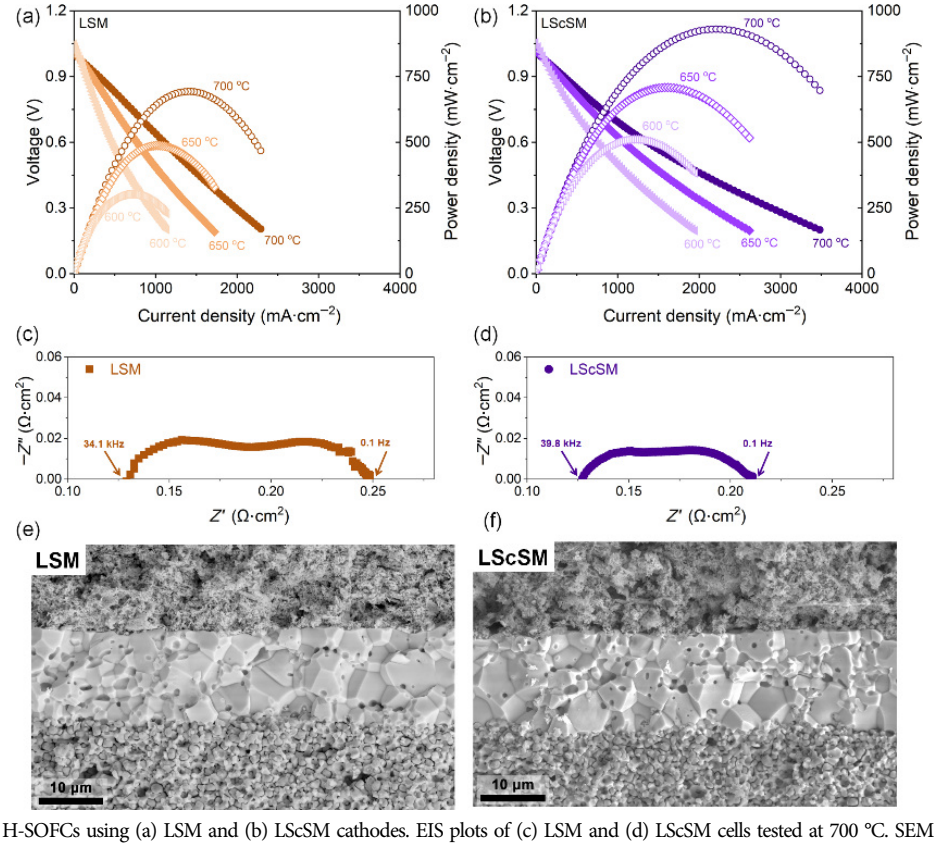

Fig. 6 Performance of H-SOFCs using (a) LSM and (b) LScSM cathodes. EIS plots of (c) LSM and (d) LScSM cells tested at 700 °C. SEM images of (e) LSM and (f) LScSM cells after testing.

implying much slower oxygen diffusion and surface exchange kinetics for $ScMnO_3$, with D_o and K_o values of 1.76×10^{-5} and 2.47×10^{-4} cm·S^{-1}, respectively. In contrast, proton diffusion and surface exchange are rapid, as indicated by the short relaxation time caused by the introduction of water into the atmosphere. The D_H and k_H values of $ScMnO_3$ are 9.98×10^{-5} and 1.08×10^{-3} cm·S^{-1}, respectively, which are significantly greater than those of LScSM under the same conditions. These findings are somewhat compatible with the previous experimental and DFT calculation results. Given its low $E_{hydration}$ value and rapid proton diffusion rate, $ScMnO_3$ appears to be a promising candidate for H-SOFC applications. Therefore, the performance of H-SOFCs employing the $ScMnO_3$ cathode was examined.

Figure 8(a) depicts the performance of H-SOFC with the $ScMnO_3$ cathode. PPD of the cell was determined to be 491, 695, and 902 mW·cm^{-2} at 600, 650, and 700 °C, respectively. Although the performance is not poor, $ScMnO_3$ does not compare adequately to other high-performance cathodes when it is employed alone [60–62]. The resistance of the $ScMnO_3$ cell was evaluated via EIS, as shown in Fig. 8(b), and the results indicate that R_o is 0.14, and R_p is 0.099 Ω·cm^2 at 700 °C. The relatively low performance is likely due to the low Vo content and sluggish oxygen diffusion kinetics, resulting in a relatively large R_p. However, some research suggests that the cathode could perform well in H-SOFCs even if its oxygen diffusion is low, assuming excellent protonation. It is known from the reaction mechanism of H-SOFCs that the proton passes through the electrolyte and reaches the cathode side [63]. If the cathode material has sufficient protonation, the proton can continue to move in the cathode and then react with O_2 at the cathode surface. In this case, the cathode reaction active area can be extended to the entire cathode surface even if the cathode has poor oxygen diffusion ability [64]. Given the low $E_{hydration}$ and high proton diffusion kinetics of $ScMnO_3$, other parameters may influence the cathode performance in addition to the Vo content and oxygen transport kinetics. Notably, R_o of the $ScMnO_3$ cell is greater than those of LSM and LScSM cells, suggesting that cathode conduction may be poor. Figure 8(c) depicts the electrical conductivity of $ScMnO_3$ together with LScSM. At intermediate temperatures, the conductivity of $ScMnO_3$ is measured to be around 1×10^{-2} S·cm^{-1}, which is significantly lower than the conductivity necessary for SOFC electrodes [65]. The comparatively poor cathode performance of $ScMnO_3$ could also be due to its extremely low conductivity. In contrast, the LScSM exhibited large conductivities at intermediate temperatures, reaching a few hundred S·cm^{-1}. A cross-sectional view of the $ScMnO_3$ cell is shown in Fig. 8(d). This cell has microstructures similar to those of the other cells in this study.

Notably, while the performances of the LScSM and $ScMnO_3$ cells are comparable, they are influenced by distinct factors. LScSM has a large Vo content, fast oxygen diffusion kinetics, and high conductivity, but its hydration ability and proton diffusion kinetics are lower than those of $ScMnO_3$. Compared with LScSM, $ScMnO_3$ has a poorer Vo content, slower oxygen transport kinetics, and lower conductivity. However, its good protonation and proton diffusion abilities can compensate for the disadvantages of LScSM. As a result, combining LScSM and

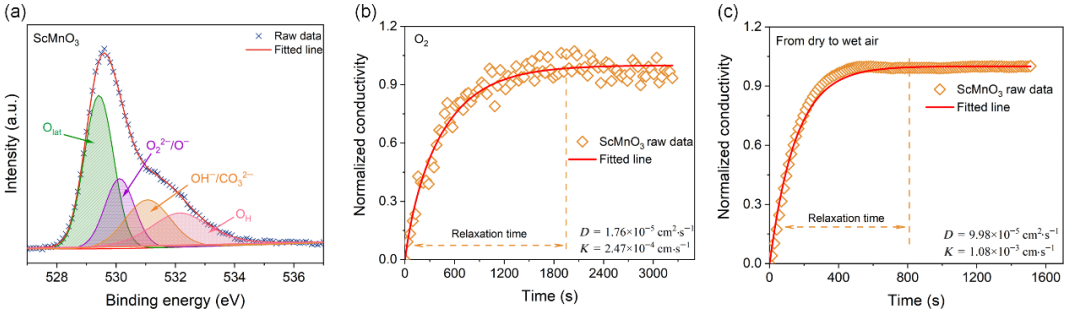

Fig. 7 (a) XPS O 1s curve for $ScMnO_3$. ECR curves tested at 600 °C for $ScMnO_3$ in atmosphere changed with (b) partial pressure of oxygen and (c) partial pressure of water.

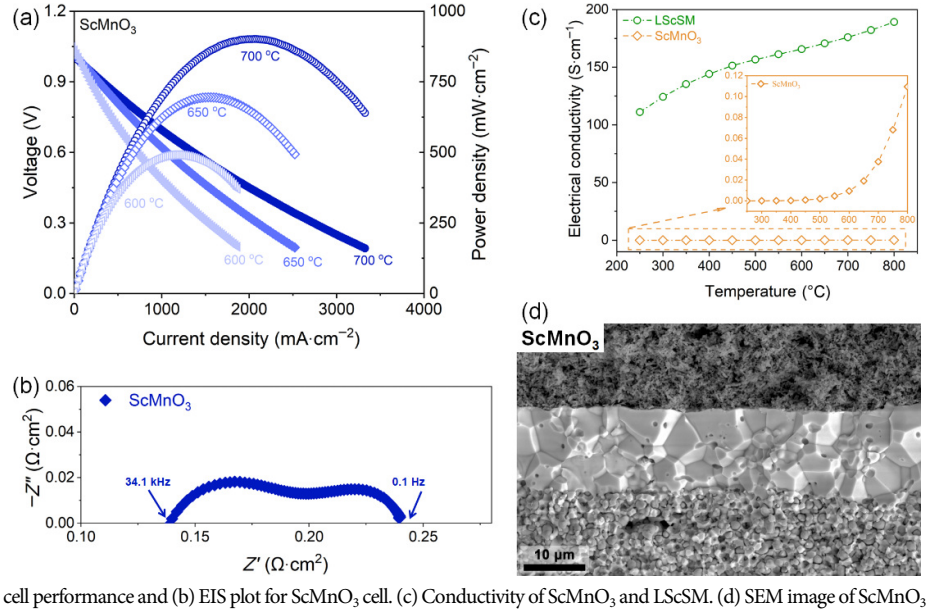

Fig. 8 (a) Fuel cell performance and (b) EIS plot for $ScMnO_3$ cell. (c) Conductivity of $ScMnO_3$ and LScSM. (d) SEM image of $ScMnO_3$ cell after testing.

$ScMnO_3$ by leveraging their respective benefits is feasible, making the evaluation of the performance of LSc5SM, LSc10SM, and LSc20SM, which are composites of LScSM+$ScMnO_3$, fascinating.

Figures 9(a)–9(c) depict the performance of H-SOFCs with LSc5SM, LSc10SM, and LSc20SM cathodes. The LSc_5SM cell has PPDs of 608, 919, and 1255 mW·cm^{-2} at 600, 650, and 700 °C, respectively. The performance is superior to that of cells employing the LScSM or $ScMnO_3$ cathode alone, demonstrating that the synergistic effect of LScSM and $ScMnO_3$ improves cell performance. The performance of the LSc10SM cell is further enhanced with PPDs of 732, 1117, and 1529 mW·cm^{-2} at 600, 650, and 700 °C, respectively, indicating that good protonation and proton diffusion abilities continue to increase the cathode performance when the Sc-doping concentration approaches 10 mol%. However, the performance of LSc20SM has not increased further. PPDs of the LSc20SM cell are 538, 821, and 1156 mW·cm^{-2} at 600, 650, and 700 °C, respectively, which are lower than those of the LS10SM cell, suggesting that an overabundance of $ScMnO_3$ degrades the overall cell performance. Figures 9(d)–9(f) show SEM images of the LSc5SM, LSc10SM, and LSc20SM cells following testing. All three cells have similar microstructures, indicating that the differences in performance cannot be attributed mainly to microstructure concerns. Cell resistance was further investigated. Figures 9(g)–9(i) show the EIS plots for the cells with the LSc5SM, LSc10SM, and LSc20SM cathodes. The R_o values are 0.126, 0.123, and 0.128 Ω·cm^2 for LSc5SM, LSc10SM, and LSc20SM, respectively. Notably, R_o is similar in all three cells. Although $ScMnO_3$ has relatively poor electronic conductivity, the high conductivity of LScSM can partially compensate for it when the LScSM+$ScMnO_3$ composite cathode is established, so the low electronic conductivity of $ScMnO_3$ has little effect on the R_o of the cells. The R_p values for LSc5SM, LSc10SM, and LSc20SM differ significantly, corresponding to values of 0.058, 0.045, and 0.065 Ω·cm^2, respectively. The use of an LScSM+$ScMnO_3$ composite cathode results in lower R_p values than those of a pure-phase LScSM or $ScMnO_3$. However, the variable LScSM and $ScMnO_3$ ratios in the composite cathode considerably impact the cathode activity and thus R_p.

Figure 10 shows SEM images of the cathode/electrolyte

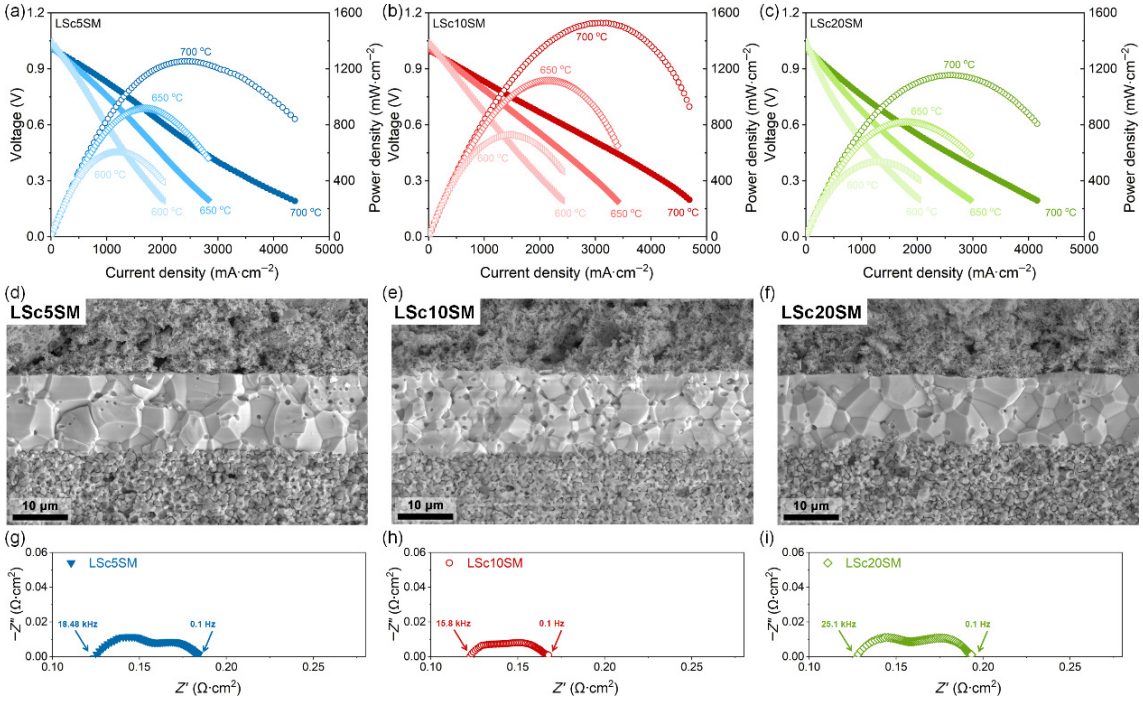

Fig. 9 Fuel cell performance, microstructures, and EIS plots tested at 700 °C for H-SOFCs with LSc5SM, LSc10SM, and LSc20SM cathodes.

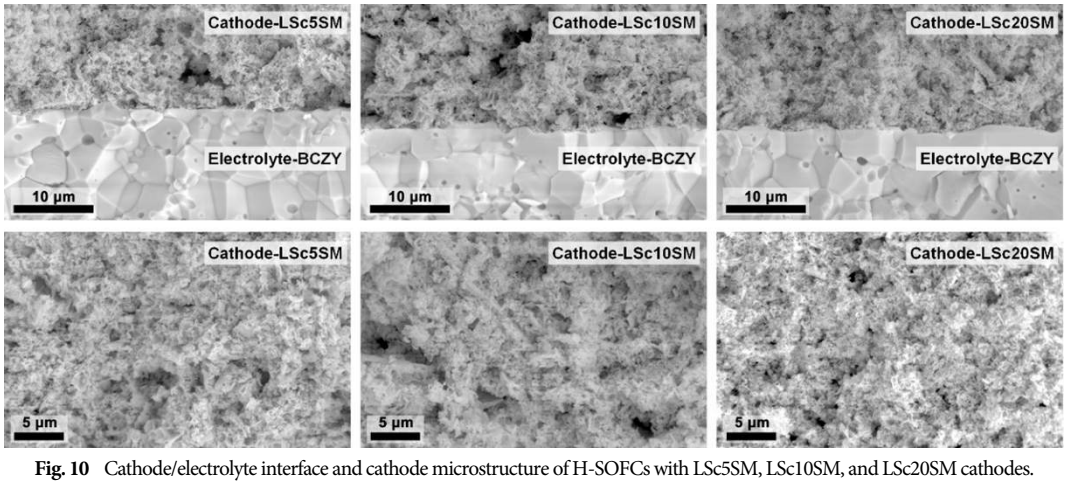

Fig. 10 Cathode/electrolyte interface and cathode microstructure of H-SOFCs with LSc5SM, LSc10SM, and LSc20SM cathodes.

interface and the cathode for H-SOFCs using the LSc5SM, LSc10SM, and LSc20SM cathodes. One can see that the cathode layer connects well to the electrolyte layer even after fuel cell testing. The different ratios of LScSM and $ScMnO_3$ do not seem to influence the good thermal compatibility between the cathode and the electrolyte, probably because of the matchable thermal expansion of the manganate cathodes with the electrolytes [66]. In addition, the LSc5SM, LSc10SM, and LSc20SM cathodes exhibit similar microstructures, suggesting that the different R_p values are due to the different cathode catalytic activities rather than microstructure issues.

Figure 11 depicts the cathode reactions of LSc5SM, LSc10SM, and LSc20SM. Although all three materials are composed of LScSM+$ScMnO_3$, the reactions vary due to the varying LScSM and $ScMnO_3$ ratios. Because the $ScMnO_3$ phase is small in LSc5SM, the majority of the reactions occur at the LScSM site. Since proton diffusion in LScSM is slow, the presence of $ScMnO_3$ can aid in proton diffusion throughout the cathode, hence resolving the bottleneck problem. When the $ScMnO_3$ concentration is low, it has no effect on the overall conductivity or oxygen diffusion ability of the cathode, resulting in better performance. By increasing the Sc doping level in LSc10SM, the amount of produced $ScMnO_3$ increases in the LScSM+$ScMnO_3$ composite, which, in theory, increases the degree of cathode proton diffusion but decreases the conductivity and oxygen transport ability. The preceding electrochemical measurements show that the performance of the LS10SM cathode remains greater than that of the LS5SM cathode, demonstrating that an increase in proton diffusion is preferable and may compensate for the loss of conductivity and oxygen diffusion ability. However, when the Sc-doping level is increased to 20 mol%, more $ScMnO_3$ is generated for LSc20SM, reducing the local conductivity and oxygen diffusion capacity of the cathode while improving the proton transport ability. The enhanced proton transport cannot fully compensate for the decreased conductivity and oxygen diffusion capacity, resulting in reduced cathode catalytic activity. It can be concluded that a suitable amount of $ScMnO_3$ in the LScSM+$ScMnO_3$ composite can increase cathode performance, but too much $ScMnO_3$ has a detrimental influence.

In addition to outstanding cell output performance, the good stability of the fuel cell is desirable. Therefore, the chemical stability of the cathode material was examined. As LSc10SM consists of LScSM and $ScMnO_3$, the chemical stabilities of LScSM, $ScMnO_3$, and LSc10SM in CO_2 and H_2O are examined, and the results are shown in Fig. 12. The LScSM, $ScMnO_3$, and LSc10SM powders were treated in a 10% CO_2-containing atmosphere or 30% H_2O-containing atmosphere, and XRD was used to examine the phase of the powders before and after the treatments. No extra phase can be detected for any of the three materials after treatment, suggesting good stability of LScSM, $ScMnO_3$, and LSc10SM in CO_2 and H_2O.

Additionally, the chemical compatibility between the LSc10SM cathode and the BCZY electrolyte material was examined, and the results revealed good chemical compatibility between these two materials. The LSc10SM powder was co-fired together with the BCZY electrolyte powder at 900 °C, which was the cathode

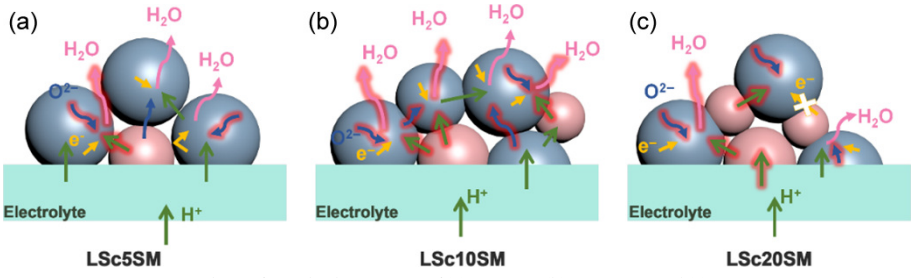

Fig. 11 Scheme for cathode reactions of (a) LSc5SM, (b) LSc10SM, and (c) LSc20SM.

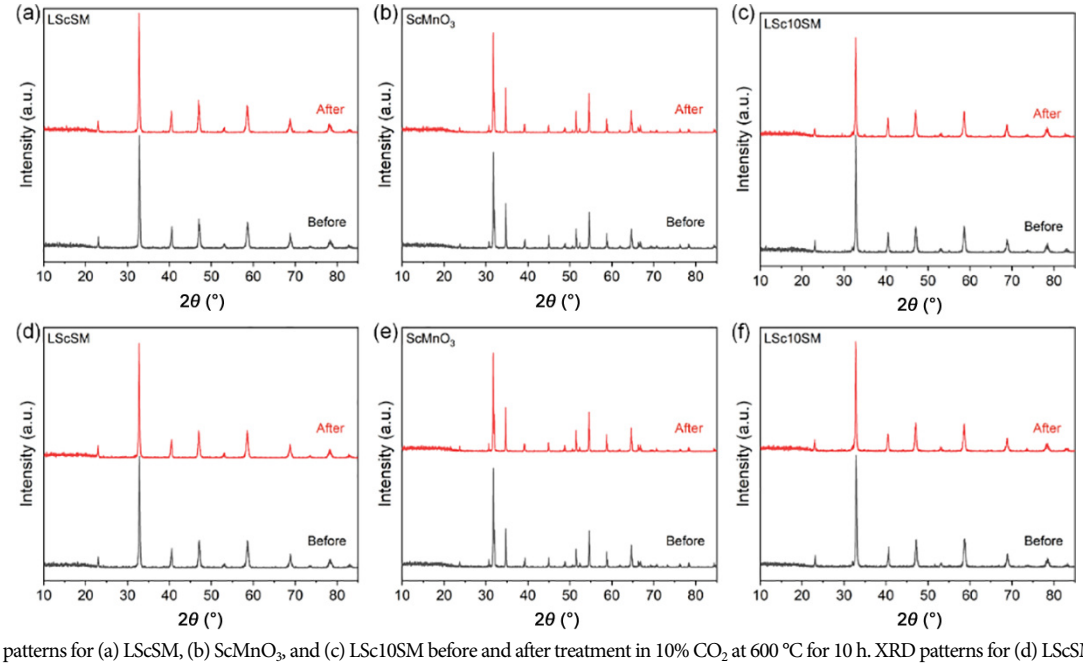

Fig. 12 XRD patterns for (a) LScSM, (b) $ScMnO_3$, and (c) LSc10SM before and after treatment in 10% CO_2 at 600 °C for 10 h. XRD patterns for (d) LScSM, (e) $ScMnO_3$, and (f) LSc10SM before and after treatment in 30% H_2O at 600 °C for 10 h.

fabrication temperature. XRD was used to examine the phase of the composite powder before and after co-firing, and the results are shown in Fig. 13(a). No extra peak can be observed for the powder after co-firing, suggesting that there is no reaction between LSc10SM and BCZY at the cathode co-firing temperature. A further examination was carried out to determine the long-term chemical compatibility between LSc10SM and BCZY at the H-SOFC working temperature. The LSc10SM+BCZY composite powder was heated at the fuel cell working temperature (600 °C) for 100 h, and XRD was used to examine the possible phase change after co-firing. The result is shown in Fig. 13(b), and one can see that the LSc10SM and BCZY structures remain unchanged. Furthermore, no new phase was observed, indicating that no reaction occurred between LSc10SM and BCZY even after 100 h of treatment at 600 °C. This result further confirms the good chemical compatibility between LSc10SM and BCZY in fuel cell applications. Because of the good chemical stability and compatibility of LSc10SM, it is reasonable to predict that the fuel cell with the LSc10SM cathode can exhibit sufficient stability under working conditions. The operational stability of the fuel cell with the LSc10SM cathode was subsequently tested, and the findings are shown in Fig. 13(c). There was no visible degradation in the cell after more than 100 h of continuous operation with the LSc10SM cathode, indicating that the cell was stable under working conditions. The superior stability and outstanding electrochemical performance make LSc10SM an ideal cathode for H-SOFCs. The Sc-doping strategy has been recognized as effective in several studies with the B site doping in ABO_3 perovskite oxides, which can improve the oxygen reduction reaction (ORR) ability of the cathode and sometimes can increase protonation. Although the doping of Sc at the A site has rarely been reported, the present study shows that doping Sc at the A site can also be helpful for improving the performance of traditional LSM cathodes, which may be employed for other cathodes. Additionally, the low solubility of Sc at the A site may generate a secondary phase, which can be used for the design of nanocomposite cathodes for H-SOFCs.

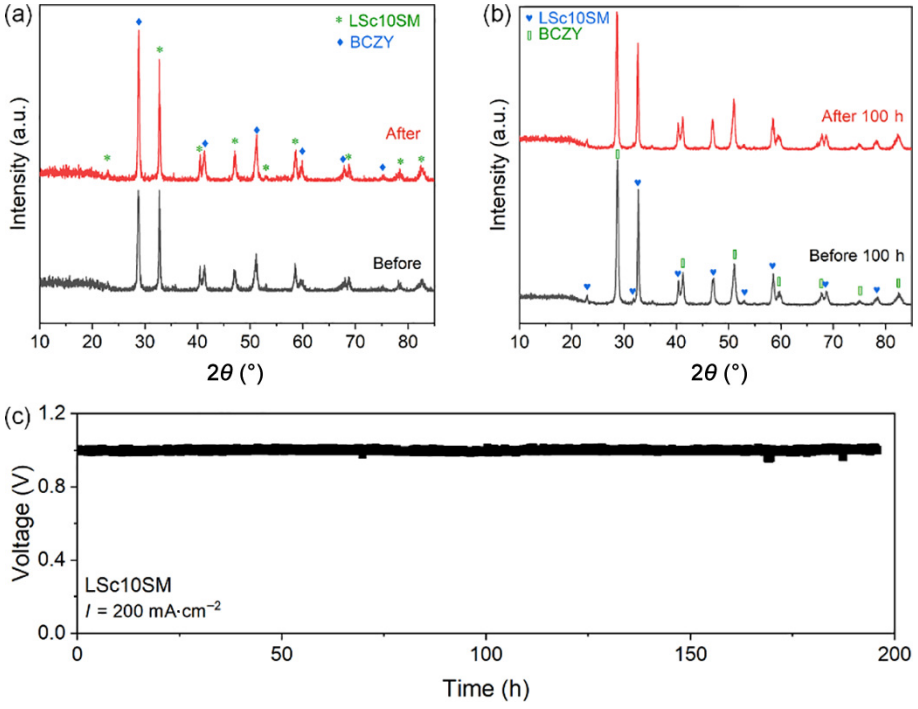

Fig. 13 XRD patterns of LSc10SM+BCZY powder before and after co-firing at (a) 900 °C for 10 min and (b) 600 °C for 100 h. (c) Operational stability of the LSc10SM cell tested at 600 °C with a constant current density (I) of 200 mA·cm^{-2}.

4 Conclusions

In this study, Sc was employed as a dopant to modify classic LSMs by replacing some La atoms. The solubility of Sc in LSM was limited to 2.5%, and additional doping of Sc can result in the synthesis of $ScMnO_3$ as the secondary phase, forming the LScSM+$ScMnO_3$ composite oxide. Despite the low Sc concentration of LSM, the newly produced LScSM oxide showed superior oxygen and proton transport capacities to those of LSM, enabling higher performance of H-SOFCs using the LScSM cathode than those using the LSM cathode. However, the performance of the cell using the pure-phase LScSM cathode remains inferior to that of recently constructed high-performance H-SOFC cathodes. $ScMnO_3$ was the secondary phase during the synthesis of $La_{0.5-x}Sc_xSr_{0.5}MnO_{3-\delta}$ when the x value was greater than 0.025, but it showed good protonation. Furthermore, the drawbacks of $ScMnO_3$, such as low electronic conductivity and slow oxygen diffusion rates, were compensated by pure-phase LScSM, whereas the slow proton diffusion kinetics of LScSM can be mitigated with $ScMnO_3$, making the LScSM+$ScMnO_3$ composite cathode an interesting candidate for H-SOFCs. The LScSM+$ScMnO_3$ composite cathodes demonstrated an apparent synergistic effect, enhancing fuel cell performance and outperforming fuel cells employing only LScSM or $ScMnO_3$ cathodes. The LSc10SM cathode was discovered to have an ideal composition, with the ratio of LScSM and $ScMnO_3$ effectively balancing electronic conduction, proton diffusion, and oxygen diffusion, resulting in a high fuel cell output of 1529 mW·cm^{-2} at 700 °C, along with excellent operational stability.

Acknowledgements

This work was supported by the National Natural Science

Foundation of China (Grant Nos. 52302314, 52272216, and 12274361).

Declaration of competing interest

The authors have no competing interests to declare that are relevant to the content of this article.

References

[1] Zhang F, Liao T, Yan C, *et al.* Bioinspired designs in active metal-based batteries. *Nano Res* 2024, **17**: 587–601.

[2] Zhu JX, Wen HY, Zhang H, *et al.* Recent advances in biodegradable electronics- from fundament to the next-generation multi-functional, medical and environmental device. *Sustain Mater Technol* 2023, **35**: e00530.

[3] Zhang F, Liao T, Qi DC, *et al.* Zn-ion ultrafluidity via bioinspired ion channel for ultralong lifespan Zn-ion battery. *Natl Sci Rev* 2024, **11**: nwae199.

[4] Ma CJ, He LH, Bi L, *et al.* Enhanced conductivity and stability of $Co_{0.98}Cu_xMn_{2.02-x}O_4$ ceramics with dual phases and twin structures. *J Adv Ceram* 2023, **12**: 1742–1757.

[5] Zhang SJ, Lan D, Chen XL, *et al.* Three-dimensional macroscopic absorbents: From synergistic effects to advanced multifunctionalities. *Nano Res* 2024, **17**: 1952–1983.

[6] Tang ZM, Liu Y, Shi KY, *et al.* Low-temperature microwave solidification of soil with radioactive tailings for sustainable applications. *Sustain Mater Technol* 2022, **31**: e00392.

[7] Qiu P, Li C, Liu B, *et al.* Materials of solid oxide electrolysis cells for H_2O and CO_2 electrolysis: A review. *J Adv Ceram* 2023, **12**: 1463–1510.

[8] Thyssen VV, Vilela VB, de Florio DZ, *et al.* Direct conversion of methane to C2 hydrocarbons in solid-state membrane reactors at high temperatures. *Chem Rev* 2022, **122**: 3966–3995.

[9] Yao W, Chen ZW, Zhang X, *et al.* Lithiophilic V_2CT_x/MoO_3 hosts with electronic/ionic dual conductive gradients for ultrahigh-rate lithium metal anodes. *Adv Funct Mater* 2024: 2400348.

[10] Lyu Y, Yuwono JA, Wang PT, *et al.* Organic pH buffer for dendrite-free and shuttle-free Zn–I_2 batteries. *Angew Chem Int Edit* 2023, **62**: 202303011.

[11] Zhang Y, Chen B, Guan DQ, *et al.* Thermal-expansion offset for high-performance fuel cell cathodes. *Nature* 2021, **591**: 246–251.

[12] Hu HB, Li MZ, Min HH, *et al.* Enhancing the catalytic activity and coking tolerance of the perovskite anode for solid oxide fuel cells through *in situ* exsolution of co-Fe nanoparticles. *ACS Catal* 2022, **12**: 828–836.

[13] Wang H, Osmieri L, Yu HR, *et al.* Elucidating the impact of the ionomer equivalent weight on a platinum group metal-free PEMFC cathode via oxygen limiting current. *SusMat* 2023, **3**: 72–90.

[14] Boldrin P, Brandon NP. Progress and outlook for solid oxide fuel cells for transportation applications. *Nat Catal* 2019, **2**: 571–577

[15] Song T, Xia T, Sun LP, *et al.* Electrochemical activity of copper doped $Sr_{2.7}Pr_{0.3}Fe_2O_{7-\delta}$ cathode catalysts for solid oxide fuel cells. *Ceram Int* 2023, **49**: 35812–35820.

[16] Wang JC, Zhao K, Zhao JS, *et al.* A NiMo-YSZ catalyst support layer for regenerable solid oxide fuel cells running on isooctane. *Appl Energ* 2022, **326**: 119907.

[17] Li YF, Xu YS, Yin YR, *et al.* Entropy engineering design of high-performing lithiated oxide cathodes for proton-conducting solid oxide fuel cells. *J Adv Ceram* 2023, **12**: 2017–2031.

[18] Gao Y, Ling YH, Wang XX, *et al.* Sr-deficient medium-entropy $Sr_{1-x}Co_{0.5}Fe_{0.2}Ti_{0.1}Ta_{0.1}Nb_{0.1}O_{3-\delta}$ cathodes with high Cr tolerance for solid oxide fuel cells. *Chem Eng J* 2024, **479**: 147665.

[19] Yang Y, Chen ZP, Li MF, *et al.* A highly efficient bismuth substitution induced A-site ordered layered perovskite electrode for symmetrical solid oxide fuel cells. *J Mater Chem A* 2023, **11**: 7995–8002.

[20] Machado M, Baiutti F, Bernadet L, *et al.* Functional thin films as cathode/electrolyte interlayers: A strategy to enhance the performance and durability of solid oxide fuel cells. *J Mater Chem A* 2022, **10**: 17317–17325.

[21] Kilner JA, Burriel M. Materials for intermediate-temperature solid-oxide fuel cells. *Annu Rev Mater Res* 2014, **44**: 365–393.

[22] Han X, Ling YH, Yang Y, *et al.* Utilizing high entropy effects for developing chromium-tolerance cobalt-free cathode for solid oxide fuel cells. *Adv Funct Mater* 2023, **33**: 2304728.

[23] Zvonareva I, Fu XZ, Medvedev D, *et al.* Electrochemistry and energy conversion features of protonic ceramic cells with mixed ionic-electronic electrolytes. *Energ Environ Sci* 2022, **15**: 439–465.

[24] Liu F, Deng H, Ding HP, *et al.* Process-intensified protonic ceramic fuel cells for power generation, chemical production, and greenhouse gas mitigation. *Joule* 2023, **7**: 1308–1332.

[25] Zhou MY, Liu ZJ, Chen ML, *et al.* Electrochemical performance and chemical stability of proton-conducting $BaZr_{0.8-x}Ce_xY_{0.2}O_{3-\delta}$ electrolytes. *J Am Ceram Soc* 2022, **105**: 5711–5724.

[26] Chen M, Xie XB, Guo JH, *et al.* Space charge layer effect at the platinum anode/$BaZr_{0.9}Y_{0.1}O_{3-\delta}$ electrolyte interface in proton ceramic fuel cells. *J Mater Chem A* 2020, **8**: 12566–12575.

[27] Chen M, Chen DC, Wang K, *et al.* Densification and electrical conducting behavior of $BaZr_{0.9}Y_{0.1}O_{3-\delta}$ proton conducting ceramics with NiO additive. *J Alloys Compd* 2019, **781**: 857–865.

[28] Han DL, Liu X, Bjørheim TS, *et al.* Yttrium-doped barium zirconate-cerate solid solution as proton conducting electrolyte: Why higher cerium concentration leads to better performance for fuel cells and electrolysis cells. *Adv Energy Mater* 2021, **11**: 2003149.

[29] Yin YR, Wang YF, Yang N, *et al.* Unveiling the importance of the interface in nanocomposite cathodes for proton-conducting solid oxide fuel cells. *Exploration* 2024, **4**: 20230082.

[30] Wang N, Yuan BY, Zheng FY, *et al.* Machine-learning assisted screening proton conducting Co/Fe based oxide for the air electrode of protonic solid oxide cell. *Adv Funct Mater* 2024, **34**: 2309855.

[31] Zou PM, Iuga D, Ling SL, *et al.* A fast ceramic mixed OH^-/H^+ ionic conductor for low temperature fuel cells. *Nat Commun* 2024, **15**: 909.

[32] Liu F, Deng H, Diercks D, *et al.* Lowering the operating temperature of protonic ceramic electrochemical cells to 450 ℃. *Nat Energy* 2023, **8**: 1145–1157.

[33] Kim JH, Kim D, Ahn S, *et al.* An universal oxygen electrode for reversible solid oxide electrochemical cells at reduced temperatures. *Energ Environ Sci* 2023, **16**: 3803–3814.

[34] Huan DM, Zhang L, Zhu K, *et al.* Improving Ruddlesden–Popper electrocatalysts through interstitial fluorination-driven rearrangements of local coordination environment. *Sustain Mater Technol* 2023, **38**: e00754.

[35] Ding HP, Wu W, Jiang C, *et al.* Self-sustainable protonic ceramic electrochemical cells using a triple conducting electrode for hydrogen and power production. *Nat Commun* 2020, **11**: 1907.

[36] Zhu ZY, Zhou MY, Fan ZD, *et al.* Improving electrocatalytic activity of cobalt-free Barium ferrite-based perovskite oxygen electrodes for proton-conducting solid oxide cells via introducing A-site deficiency. *ACS Appl Energ Mater* 2023, **6**: 5155–5166.

[37] Liu ZQ, Bai YS, Sun HN, *et al.* Synergistic dual-phase air electrode enables high and durable performance of reversible proton ceramic electrochemical cells. *Nat Commun* 2024, **15**: 472.

[38] Yin YR, Zhang SQ, Wang A, *et al.* Rational design of $PrBaFe_2O_{6-\delta}$-based cathodes for protonic ceramic fuel cells. *J Adv Ceram* 2024, **13**: 1600–1610.

[39] Yin YR, Liu B, Yan D, *et al.* Balancing intrinsic properties of cathode materials allows high performance for protonic ceramic fuel cells. *SusMat* 2024: e240.

[40] Xu YS, Gu YY, Bi L. A highly-active $Zn_{0.58}Co_{2.42}O_4$ spinel oxide as a promising cathode for proton-conducting solid oxide fuel cells. *J Mater Chem A* 2022, **10**: 25437–25445.

[41] Graves C, Ebbesen SD, Jensen SH, *et al.* Eliminating degradation in solid oxide electrochemical cells by reversible operation. *Nat Mater* 2015, **14**: 239–244.

[42] Wu S, Xu X, Li XM, *et al.* High-performance proton-conducting solid oxide fuel cells using the first-generation Sr-doped $LaMnO_3$ cathode tailored with Zn ions. *Sci China Mater* 2022, **65**: 675–682.
[43] Dai HL, Yin YR, Li XM, *et al.* A new Sc-doped $La_{0.5}Sr_{0.5}MnO_{3-\delta}$ cathode allows high performance for proton-conducting solid oxide fuel cells. *Sustain Mater Technol* 2022, **32**: e00409.
[44] Ji QQ, Bi L, Zhang JT, *et al.* The role of oxygen vacancies of ABO_3 perovskite oxides in the oxygen reduction reaction. *Energ Environ Sci* 2020, **13**: 1408–1428.
[45] Zhou R, Yin YR, Dai HL, *et al.* Attempted preparation of $La_{0.5}Ba_{0.5}MnO_{3-\delta}$ leading to an *in-situ* formation of manganate nanocomposites as a cathode for proton-conducting solid oxide fuel cells. *J Adv Ceram* 2023, **12**: 1189–1200.
[46] Kresse G, Furthmüller J. Efficient iterative schemes for *ab initio* total-energy calculations using a plane-wave basis set. *Phys Rev B* 1996, **54**: 11169–11186.
[47] Yang X, Yin YR, Yu SF, *et al.* Gluing $Ba_{0.5}Sr_{0.5}Co_{0.8}Fe_{0.2}O_{3-\delta}$ with Co_3O_4 as a cathode for proton-conducting solid oxide fuel cells. *Sci China Mater* 2023, **66**: 955–963.
[48] Muñoz-García AB, Tuccillo M, Pavone M. Computational design of cobalt-free mixed proton–electron conductors for solid oxide electrochemical cells. *J Mater Chem A* 2017, **5**: 11825–11833.
[49] Yin YR, Dai HL, Yu SF, *et al.* Tailoring cobalt-free $La_{0.5}Sr_{0.5}FeO_{3-\delta}$ cathode with a nonmetal cation-doping strategy for high-performance proton-conducting solid oxide fuel cells. *SusMat* 2022, **2**: 607–616.
[50] Zhang XH, Pei CL, Chang X, *et al.* FeO_6 octahedral distortion activates lattice oxygen in perovskite ferrite for methane partial oxidation coupled with CO_2 splitting. *J Am Chem Soc* 2020, **142**: 11540–11549.
[51] Zhang LL, Yin YR, Xu YS, *et al.* Tailoring $Sr_2Fe_{1.5}Mo_{0.5}O_{6-\delta}$ with Sc as a new single-phase cathode for proton-conducting solid oxide fuel cells. *Sci China Mater* 2022, **65**: 1485–1494.
[52] Liu B, Li ZB, Yang XW, *et al.* Novel mixed $H^+/e^-/O^{2-}$ conducting cathode material $PrBa_{0.9}K_{0.1}Fe_{1.9}Zn_{0.1}O_{5+\delta}$ for proton-conducting solid oxide fuel cells. *J Mater Chem A* 2022, **10**: 17425–17433.
[53] Ren RZ, Wang ZH, Meng XG, *et al.* Tailoring the oxygen vacancy to achieve fast intrinsic proton transport in a perovskite cathode for protonic ceramic fuel cells. *ACS Appl Energ Mater* 2020, **3**: 4914–4922.
[54] Li YF, Yu SF, Dai HL, *et al.* TiO_2-induced electronic change in traditional $La_{0.5}Sr_{0.5}MnO_{3-\delta}$ cathode allows high performance of proton-conducting solid oxide fuel cells. *Sci China Mater* 2023, **66**: 3475–3483.
[55] Fu M, Lin X, Tan LG, *et al.* Self-assembled Fe-doped $PrBaCo_2O_{5+\delta}$ composite cathodes with disorder transition region for intermediate-temperature solid oxide fuel cells. *Int J Hydrog Energ* 2023, **48**: 15229–15237.
[56] Yu ZX, Ge L, Ni Q, *et al.* Superior durability and activity of a benchmark triple-conducting cathode by tuning thermo–mechanical compatibility for protonic ceramic fuel cells. *Adv Funct Mater* 2024, **34**: 2309698.
[57] Zhou R, Gu YY, Dai HL, *et al.* *In-situ* exsolution of PrO_{2-x} nanoparticles boost the performance of traditional $Pr_{0.5}Sr_{0.5}MnO_{3-\delta}$ cathode for proton-conducting solid oxide fuel cells. *J Eur Ceram Soc* 2023, **43**: 6612–6621.
[58] Xu YS, Yu SF, Yin YR, *et al.* Taking advantage of Li-evaporation in $LiCoO_2$ as cathode for proton-conducting solid oxide fuel cells. *J Adv Ceram* 2022, **11**: 1849–1859.
[59] Song YF, Chen YB, Wang W, *et al.* Self-assembled triple-conducting nanocomposite as a superior protonic ceramic fuel cell cathode. *Joule* 2019, **3**: 2842–2853.
[60] Yin YR, Zhou YB, Gu YY, *et al.* Successful preparation of $BaCo_{0.5}Fe_{0.5}O_{3-\delta}$ cathode oxide by rapidly cooling allowing for high-performance proton-conducting solid oxide fuel cells. *J Adv Ceram* 2023, **12**: 587–597.
[61] Liang MZ, He F, Zhou C, *et al.* Nickel-doped $BaCo_{0.4}Fe_{0.4}Zr_{0.1}Y_{0.1}O_{3-\delta}$ as a new high-performance cathode for both oxygen-ion and proton conducting fuel cells. *Chem Eng J* 2021, **420**: 127717.
[62] Dai HL, Du HZ, Boulfrad S, *et al.* Manipulating Nb-doped $SrFeO_{3-\delta}$ with excellent performance for proton-conducting solid oxide fuel cells. *J Adv Ceram* 2024, **13**: 579–589.
[63] Meng YQ, Duffy J, Na BT, *et al.* Oxygen exchange and bulk diffusivity of $BaCo_{0.4}Fe_{0.4}Zr_{0.1}Y_{0.1}O_{3-\delta}$: Quantitative assessment of active cathode material for protonic ceramic fuel cells. *Solid State Ion* 2021, **368**: 115639.
[64] Yin YR, Xiao DD, Wu S, *et al.* A real proton-conductive, robust, and cobalt-free cathode for proton-conducting solid oxide fuel cells with exceptional performance. *SusMat* 2023, **3**: 697–708.
[65] Tao SW, Irvine JTS. A redox-stable efficient anode for solid-oxide fuel cells. *Nat Mater* 2003, **2**: 320–323.
[66] He SC, Yin YR, Bi L, *et al.* A new $Pr_{0.25}Nd_{0.25}Sr_{0.5}MnO_{3-\delta}$ cathode for proton-conducting solid oxide fuel cells. *Ceram Int* 2022, **48**: 11872–11878.